RSC Advances

PAPER

Cite this: *RSC Adv.*, 2015, **5**, 64651

# Nickel-promoted mesoporous ZSM5 for carbon monoxide methanation

L. P. Teh,[a] S. Triwahyono,*[ab] A. A. Jalil,[cd] C. R. Mamat,[a] S. M. Sidik,[d] N. A. A. Fatah,[d] R. R. Mukti[e] and T. Shishido[f]

Nickel-promoted mesoporous ZSM5 (Ni/mZSM5) was prepared for CO methanation. XRD, NMR and SEM analysis confirmed the structural stability of Ni/mZSM5 with coffin type morphology. The nitrogen physisorption and pyrrole adsorbed FTIR analyses indicated the presence of micro–mesoporosity and a moderate amount of basic sites on both mZSM5 and Ni/mZSM5. At 623 K, Ni/mZSM5 showed a high rate of CO conversion (141.6 μmol CO g-cat$^{-1}$ s$^{-1}$) and 92% $CH_4$ yield. Ni/mZSM5 showed better catalytic performance than Ni/MSN (82.4 μmol CO g-cat$^{-1}$ s$^{-1}$, 82% $CH_4$ yield), Ni/HZSM5 (29.0 μmol CO g-cat$^{-1}$ s$^{-1}$, 54.5% $CH_4$ yield), and Ni/γ-$Al_2O_3$ (14.5 μmol CO g-cat$^{-1}$ s$^{-1}$, 38.6% $CH_4$ yield). It is noteworthy that the superior catalytic performance of Ni/mZSM5 could be attributed to the presence of both micro–mesoporosity and basicity, which led to a synergistic effect of Ni metal active sites and the mZSM5 support. *In situ* FTIR spectroscopy showed that CO and $H_2$ may be adsorbed on Ni metal followed by spillover to form adsorbed CO and adsorbed H on the mZSM5 surface. Then, two possible mechanisms for CO methanation were proposed. In the first mechanism, the adsorbed CO may be reacted with $H_2$ to form $CH_4$ and $H_2O$. In the second mechanism, the adsorbed H may be reacted with CO to form $CH_4$ and $CO_2$. However, in this case, the former is the predominant pathway as the methanation reaction is favored by inhibition of the water–gas shift reaction.

Received 17th June 2015
Accepted 21st July 2015

DOI: 10.1039/c5ra11661a

www.rsc.org/advances

## Introduction

Methanation of carbon oxides (CO and/or $CO_2$), also known as the Sabatier reaction, has been an indispensable reaction for producing methane.[1] The catalytic conversion of syngas ($H_2$ + CO) into methane (so-called synthetic natural gas, SNG) is currently of utmost importance owing to the requirements of environmental regulations. Due to the abundance of carbon monoxide released into the atmosphere, methanation of CO has attracted increasing attention for effectively mitigating CO buildup and recycling the carbon resource.[2] Besides, the catalytic methanation of CO is also potentially an effective method of reducing the content of CO in $H_2$-rich reformate gas mixture, which is normally used in fuel cell applications.[3]

In previous reports, catalytic performances for CO methanation have been mostly investigated on various supports, such as silica, alumina, and mesoporous material.[4–10] Yan *et al.* reported the use of plasma prepared Ni/$SiO_2$ on CO methanation.[5] It gave about 82% CO conversion at 673 K. Guo *et al.* studied the effect of $ZrO_2$ in Ni/$Al_2O_3$ for CO methanation.[6] 100% CO conversion was obtained at 623 K. On the other hand, Liu *et al.* studied the influence of $V_2O_3$ in the catalytic performance of Ni/$Al_2O_3$ for CO methanation.[7] At 673 K, it showed nearly 100% CO conversion and 89% $CH_4$ yield. Moreover, Zhang *et al.* reported that 10 wt% Ni-MCM-41 exhibited excellent activity and stability in the CO methanation with 95.7% $CH_4$ yield at 623 K.[8] Besides, Gao *et al.* prepared the high surface area Ni supported on barium hexaaluminate (Ni/BHA) for improved CO methanation compared with the conventional Ni/BHA.[9] It gave 100% CO conversion and 95.7% $CH_4$ yield at 673 K. In addition, Jia *et al.* reported the improved CO methanation with the use of nickel supported on the perovskite oxide $CaTiO_3$ (Ni/CTO).[10] At 673 K, it showed 100% CO conversion and 84% $CH_4$ yield. Nevertheless, they are seldom supported on zeolites. For many catalytic reactions, structure and activity were greatly influenced by the nature of the support material.[11–14]

Zeolites have proven to be suitable for a variety of applications in industrial heterogeneous catalysis, separation, and adsorption processes. Zeolite ZSM5 is a crystalline

[a]*Department of Chemistry, Faculty of Science, Universiti Teknologi Malaysia, 81310 UTM Johor Bahru, Johor, Malaysia. E-mail: sugeng@utm.my*

[b]*Ibnu Sina Institute for Fundamental Science Studies, Universiti Teknologi Malaysia, 81310 UTM Johor Bahru, Johor, Malaysia*

[c]*Institute of Hydrogen Economy, Universiti Teknologi Malaysia, 81310 UTM Johor Bahru, Johor, Malaysia*

[d]*Department of Chemical Engineering, Faculty of Chemical Engineering, Universiti Teknologi Malaysia, 81310 UTM Johor Bahru, Johor, Malaysia*

[e]*Division of Inorganic and Physical Chemistry, Faculty of Mathematics and Natural Sciences, Institut Teknologi Bandung, Jl Ganesha No 10, Bandung 40132, Indonesia*

[f]*Department of Applied Chemistry, Graduate School of Urban Environmental Sciences, Tokyo Metropolitan University, 1-1 Minami-Osawa, Hachioji, Tokyo 192-0397, Japan*

aluminosilicate with an MFI structure. It possesses both acidic and basic sites. The bridging OH groups, the trigonally coordinated and extra framework aluminum contributed to the acidity.[15] While, the basicity is due to the basic framework oxygen atoms bearing the negative charge. The negative charge on the oxygen atoms is enhanced as the electropositive character of the nonframework compensating cations increases.[16] The extraordinary catalytic performance of zeolite catalysts is due to their crystalline frameworks and topological channel structures.[17] However, the relatively small individual micropores in zeolites cause diffusion limitations and significantly influence the transportation to and from the active site, severely limiting their application in industry. Moreover, deactivation caused by coke formation is also a severe problem that routinely arises in catalytic applications catalyzed by zeolites.[18] Therefore, mesoporous zeolites possessing micro–mesoporosity are urgently needed as an effective solution to overcome these drawbacks.

A large number of supported metal catalysts have been reported to be active for CO methanation. Various transition metals like Ni, Co, Rh, Ru, Pd, Pt, and so on have been investigated over different supports.[19,20] However, some noble metals such as Rh and Ru are not economical for large-scale production of methane due to their high cost. Therefore, the use of nickel-based catalysts is preferred from the commercial standpoint because of their low cost and wide availability. It should be noted that the catalytic performance of the nickel-based catalysts depends not only on the active nickel metal sites but also on the chemical and physical properties of the supporting materials.

In our previous work, we prepared mesoporous ZSM5 (mZSM5) by the dual templating method and tailored the zeolite properties by varying the aging time.[21] In the present work, we prepared nickel-promoted mesoporous ZSM5 (Ni/mZSM5) for CO methanation. The correlation of their physicochemical properties with the catalytic performances is presented and discussed. For comparison purposes, we also studied different types of supports such as commercial HZSM5, $\gamma$-$Al_2O_3$, and mesostructured silica nanoparticles (MSN). Moreover, *in situ* FTIR spectroscopy of CO methanation using mZSM5 and Ni/mZSM5 catalyst was also performed in order to provide deeper insight into the reaction mechanism. The high activity of structurally stable Ni/mZSM5 for CO methanation was strongly determined by the presence of both micro–mesoporosity and basicity, which led to a synergistic effect between Ni metal active sites and the mZSM5 support.

# Experimental

### Catalyst preparation

The mesoporous ZSM5 was prepared by dual templating method using tetrapropylammonium bromide (TPA-Br) as micropore directing agent and benzalkonium chloride as mesopore directing agent. The starting parameters are Si/Al = 22.90, $H_2O$/Si = 18.30, TPA-Br/Si = 0.17, benzalkonium chloride/Si = 0.06, and NaOH/Si = 0.15. Firstly, the mixture of benzalkonium chloride, tetrapropylammonium bromide (TPA-Br), sodium hydroxide (NaOH), and distilled water ($H_2O$) was homogeneously mixed at room temperature under vigorous stirring for 5 min. Then, aluminium hydroxide, $Al(OH)_3$ and tetraethyl orthosilicate (TEOS), $Si(OC_2H_5)_4$ were added and homogeneously mixed at room temperature under vigorous stirring for 3 h. After that, the mixture was transferred into autoclave and maintained at 423 K for 0.5 day. The product was washed, filtered, and drying at 383 K for 3 h. The as-synthesized catalyst was calcined at 823 K for 3 h. The prepared catalyst was denoted as mZSM5.

A commercial HZSM5 (Zeolyst International) with Si/Al atomic ratio of 23 was used as a catalyst support. A commercial $\gamma$-$Al_2O_3$ (Sigma-Aldrich) was used as a catalyst support. Prior to modification, HZSM5 and $\gamma$-$Al_2O_3$ was treated at 823 K. MSN was prepared by the sol–gel method according to a report by Aziz *et al.*[22] In brief, cetyltrimethylammonium bromide (CTAB), ethylene glycol (EG), and $NH_4OH$ solution were dissolved in water with the following molar composition of CTAB : EG : $NH_4OH$ : $H_2O$ = 0.0032 : 0.2 : 0.2 : 0.1. After vigorous stirring for about 30 min at 353 K, 1.2 mmol of tetraethyl orthosilicate and 1 mmol of 3-aminopropyl triethoxysilane were added to the clear mixture to give a white suspension solution. This solution was then stirred for another 2 h, and the sample was collected by centrifugation at 3000 rpm. The synthesized MSN was dried at 333 K and calcined at 823 K for 3 h.

The 5 wt% Ni-promoted supports were prepared by the wet impregnation method over mZSM5, HZSM5, $\gamma$-$Al_2O_3$, and MSN supports. The aqueous nickel nitrate ($Ni(NO_3)_2 \cdot 6H_2O$) was impregnated on the support at 353 K, and was then dried in an oven at 383 K overnight before calcination in air at 823 K for 3 h.

### Characterization

The crystalline structure of the catalyst was studied by X-ray diffraction (XRD) recorded on a Bruker Advance D8 X-ray powder diffractometer (40 kV, 40 mA) using Cu K$\alpha$ radiation source in the range of $2\theta$ = 2–80° with a scan rate of 0.1° continuously. The nitrogen physisorption analysis of the catalysts was carried out by using a Beckman Coulter SA 3100. Prior to the measurement, the catalyst was put into a sample tube holder, followed by evacuation at 573 K for 1 h. Then, adsorption of nitrogen was carried out at 77 K. Surface area, pore size distributions and pore volumes were determined from the sorption isotherms using a non-local density functional theory (NLDFT) method. MAS NMR spectra were obtained using a Bruker Avance 400 MHz spectrometer. $^{27}$Al MAS NMR spectra were obtained at 104.2 MHz using pulse length of 1.9 μs, spin rate of 7 kHz, and relaxation time delay of 2 s. $^{29}$Si MAS NMR spectra were recorded at a frequency of 79.4 MHz using a 4 μs radio frequency pulses, a recycle delay of 60 s and spinning rate of 7 kHz using a 4 mm zirconia sample rotor. The surface morphology of the samples was performed using scanning electron microcopy (JEOL JSM-6390LV) working at 15 kV. In the characterization of the basic properties, pyrrole has been used as a probe molecule. The CO methanation was also performed by *in situ* FTIR spectroscopy to study the surface species formed

 

during the reaction. All the measurements were performed on an Agilent Cary 640 FTIR spectrometer equipped with a high-temperature stainless steel cell with $CaF_2$ windows. Prior to the measurements, all samples were activated at 673 K for 1 h. For pyrrole adsorption, the activated catalyst was exposed to 4 Torr of pyrrole at room temperature for 5 min, followed by outgassing at room temperature, 323, 373, 423, and 473 K for 5 min. All spectra were recorded at room temperature. For CO + $H_2$ adsorption studies, the sample was activated at 673 K for 1 h followed by flowing under $H_2$ stream (10 ml $min^{-1}$) at 673 K for 1 h. The formation of surface species during the CO methanation was carried out by introducing a mixture of CO (20 Torr) and $H_2$ (160 Torr) to the catalyst at room temperature, followed by heating to 323, 373, 423, 473, 523, 573, and 623 K. For the interaction of $H_2$ with pre-adsorbed CO and interaction of CO with pre-adsorbed $H_2$ studies, the sample was activated using the same procedure as above. Firstly, the activated sample was heated in the presence of CO or $H_2$ at 623 K for 1 h in order to adsorb CO or $H_2$ on the catalyst surface. Then, the interaction of pre-adsorbed CO or $H_2$ samples with $H_2$ or CO gas was done by exposing 160 Torr of $H_2$ or 20 Torr of CO, respectively, at room temperature and subsequent heating to 623 K with the increment of 50 K from room temperature. All spectra were recorded at room temperature.

### Catalytic testing

Carbon monoxide methanation was carried out in a fixed-bed quartz reactor at temperature range of 423–673 K. Initially, 0.2 g of catalyst were treated in an oxygen stream for 1 h followed by a hydrogen stream for 3 h at 773 K and cooled down to the desired reaction temperature in a hydrogen stream. When the temperature became stable, a mixture of $H_2$ and CO was fed into the reactor at a specific gas hourly space velocity (GHSV) and $H_2$/CO mass ratio. The composition of the outlet gases was analyzed by an on-line 6090 N Agilent gas chromatograph equipped with a TCD detector. The moisture trap was installed at the outlet gas line of the reactor to prevent moisture from entering the GC. The CO conversion, $CH_4$ and $CO_2$ selectivity, $CH_4$ and $CO_2$ yield, and rate of CO conversion were calculated according to the following equations:

$$X_{CO}(\%) = \frac{M_{CH_4} + M_{CO_2}}{M_{CO} + M_{CH_4} + M_{CO_2}} \times 100 \quad (1)$$

$$S_{CH_4}(\%) = \frac{M_{CH_4}}{M_{CH_4} + M_{CO_2}} \times 100 \quad (2)$$

$$S_{CO_2}(\%) = \frac{M_{CO_2}}{M_{CH_4} + M_{CO_2}} \times 100 \quad (3)$$

$$Y_{CH_4}(\%) = \frac{X_{CO} \times S_{CH_4}}{100} \quad (4)$$

$$Y_{CO_2}(\%) = \frac{X_{CO} \times S_{CO_2}}{100} \quad (5)$$

$$\text{Rate of CO conversion}\left(\mu\text{mol CO g-cat}^{-1}\ \text{s}^{-1}\right) = \frac{n_{CO}}{W_{cat}\ \text{s}} \quad (6)$$

where, $X_{CO}$ is the conversion of carbon monoxide (%), $S_{CH_4}$ and $S_{CO_2}$ is the selectivity of $CH_4$ (%) and $CO_2$ (%), respectively, $Y_{CH_4}$ and $Y_{CO_2}$ is the yield of $CH_4$ (%) and $CO_2$ (%), respectively; $M$ is a mole of the CO, $CH_4$ or $CO_2$. The rate of CO conversion was expressed in areal rate form. The rate of CO conversion is reported as moles of CO converted (μmol CO) divided by the weight of the catalyst (g-cat) and time (s).

## Results and discussion

### Physical properties of the catalysts

Fig. 1 shows the XRD patterns of mZSM5, HZSM5, γ-$Al_2O_3$, MSN, and Ni-promoted catalysts. The typical diffraction peaks of MFI-type zeolite (ZSM5) are at $2\theta = 7–10^\circ$ and $22–25^\circ$.[23] After the introduction of Ni, the intensity of peaks of mZSM5 did not change much while that of commercial HZSM5 was slightly decreased. This indicated some minor structural degradation of commercial HZSM5. Moreover, mZSM5 possessed higher crystallinity as the intensity of peaks of mZSM5 was higher than that of commercial HZSM5. An identical XRD pattern for the predominantly γ-phase $Al_2O_3$ was observed for $Al_2O_3$-based catalysts. The XRD patterns showed no additional signals other than that of γ-phase $Al_2O_3$ at $2\theta = 37.0^\circ$, $45.7^\circ$, and $66.6^\circ$.[24,25] However, the γ-$Al_2O_3$ peaks were slightly increased upon the introduction of Ni. The slight increase in crystallinity may be

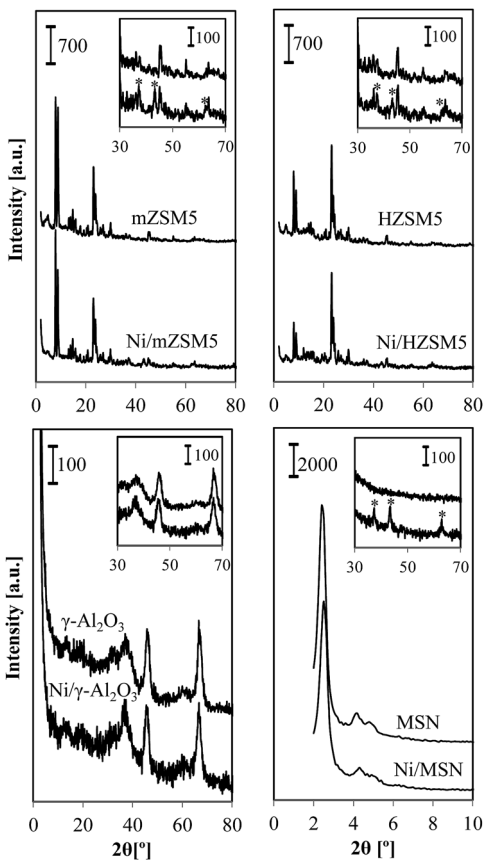


Fig. 1 XRD patterns of mZSM5, HZSM5, γ-$Al_2O_3$, MSN, and Ni-promoted catalysts; the inset shows NiO (*) peaks.

due to the elimination of distorted aluminum sites, leading to a more ordered framework structure of γ-$Al_2O_3$. In addition, it also indicated that nickel may interact with γ-$Al_2O_3$. In the case of MSN-based catalysts, there are three well-resolved Bragg diffraction peaks at $2\theta = 2.4°$, 4.0°, and 4.4°, which can be indexed as (100), (110), and (200) reflections of a hexagonal ordered mesostructure (*P6mm*), which is typical for MCM-41 type materials.[22,26] The intensity of peaks was decreased, which may be because the ordered MSN support structure was slightly disturbed by the presence of Ni. The presence of metal crystallites on the catalysts was characterized using wide-angle XRD (30–70°), as shown in the inset figure of Fig. 1. The characteristic diffraction peaks of the NiO particles at $2\theta = 37.1°$, 43.2°, and 62.7° were observed for Ni/mZSM5, Ni/HZSM5, and Ni/MSN.[27] However, no diffraction peaks of the NiO particles were observed for Ni/γ-$Al_2O_3$. This may be due to the superposition of the NiO particles' diffraction peaks with γ-$Al_2O_3$ peaks or because NiO particles are too small to be detected by XRD.

Fig. 2 shows the $N_2$ adsorption–desorption isotherms and NLDFT pore size distribution of mZSM5, HZSM5, γ-$Al_2O_3$, MSN, and Ni-promoted catalysts. For mZSM5-based catalysts (mZSM5and Ni/mZSM5), all isotherms were type IV adsorption isotherms with type H1 hysteresis loops, which is typically exhibited by uniform mesoporous material according to the IUPAC classification. A sharp uptake at low relative pressure indicated the presence of microporosity. In addition, an increased uptake at relative pressures of $P/P_0 = 0.2–0.4$ was due to the presence of mesoporosity. The first step at a relative pressure of 0.2–0.4 was due to the presence of intraparticle pores, while the second step at $P/P_0 = 0.9–1.0$ was due to the presence of interparticle pores.[28] These results confirm the permanence of the mesoporous phase in parallel with the microporous phase in mZSM5. Besides, it is noteworthy that the second step at higher partial pressure was slightly decreased for Ni/mZSM5, which could be attributed to the fact that Ni particles blocked some of the interparticle pores of mZSM5. On the contrary, commercial HZSM5 demonstrated a type I isotherm with type H4 hysteresis loops, which is usually exhibited by microporous solids.[29] No obvious changes were observed upon the introduction of Ni. For $Al_2O_3$-based catalysts (γ-$Al_2O_3$ and Ni/γ-$Al_2O_3$), all isotherms were type IV adsorption isotherms (according to the IUPAC classification) with type H1 hysteresis loops, which is characteristic of mesoporous materials, broad pore size distribution, and uniform cylindrical shape.[30,31] No significant difference was noticed for Ni/γ-$Al_2O_3$ with respect to the bare γ-$Al_2O_3$. Moreover, MSN-based catalysts (MSN and Ni/MSN) exhibited a type IV isotherm with a type H1 hysteresis loop, confirming a typical adsorption profile for a mesostructured material. The filling of intraparticle and interparticle pores was observed at $P/P_0 = 0.2–0.4$ and 0.9–1.0, respectively. The decrease of the step at high partial pressure could be attributed to the fact that the Ni particles blocked the interparticle pores of MSNs.

The pore size distribution of all catalysts was calculated by the non-local density functional theory (NLDFT) method. Significantly, narrow pore size distributions in the range of 3–6 nm were observed for mZSM5. It is noteworthy that mZSM5 has both micropores and mesopores and the amount of mesopores is higher than in commercial HZSM5. With Ni–metal loading, the pore size of the mZSM5 shifted towards a higher occurrence of micropores and slightly higher mesopore size. For HZSM5, an obvious decrease of the pore volume at a pore size of 2.4 nm led to the evolution of smaller observed pore size after the introduction of Ni onto HZSM5. For $Al_2O_3$-based catalysts, the pore size distribution was centered at 9.4 nm. Only

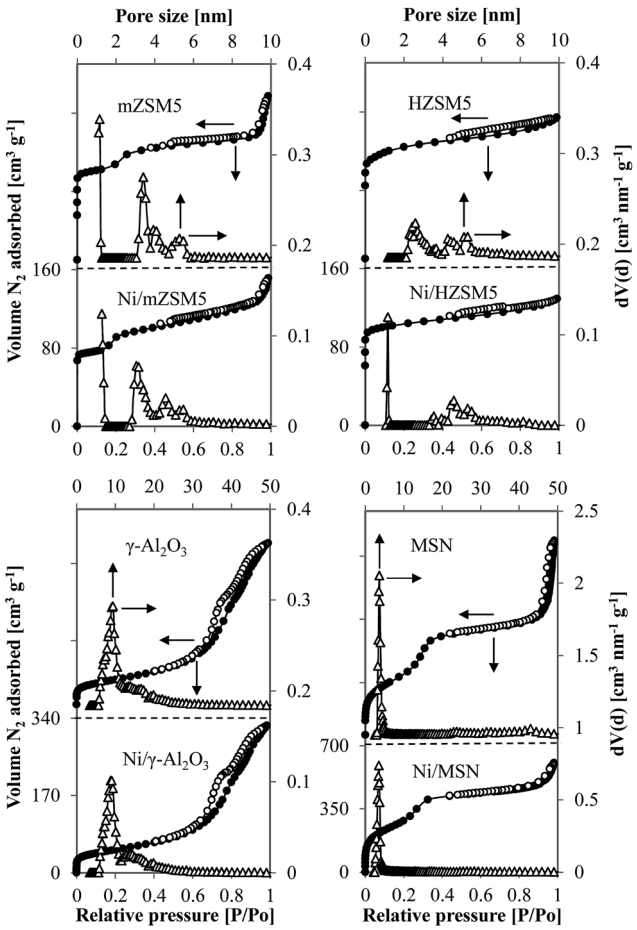


Fig. 2 $N_2$ adsorption–desorption isotherms and NLDFT pore size distribution of mZSM5, HZSM5, γ-$Al_2O_3$, MSN, and Ni-promoted catalysts.

Table 1 Textural properties of mZSM5, HZSM5, γ-$Al_2O_3$, MSN, and Ni-promoted catalysts

| Catalysts | Surface area ($m^2$ $g^{-1}$) | Total pore volume ($cm^3$ $g^{-1}$) |
|---|---|---|
| mZSM5 | 733 | 0.248 |
| Ni/mZSM5 | 477 | 0.203 |
| HZSM5 | 389 | 0.222 |
| Ni/HZSM5 | 367 | 0.199 |
| γ-$Al_2O_3$ | 198 | 0.531 |
| Ni/γ-$Al_2O_3$ | 184 | 0.485 |
| MSN | 965 | 1.573 |
| Ni/MSN | 769 | 0.867 |

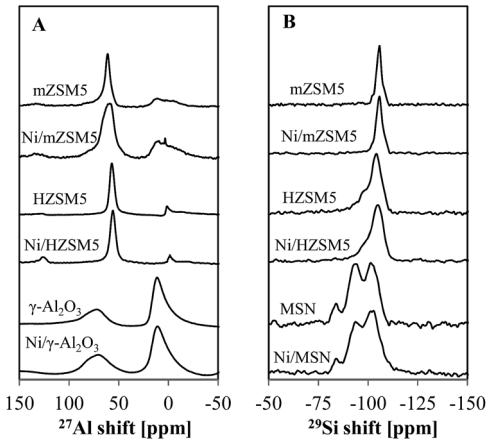


Fig. 3 (A) $^{27}$Al MAS NMR and (B) $^{29}$Si MAS NMR spectra of all catalysts.

a slight decrease in the pore volume was observed on Ni/γ-$Al_2O_3$. For MSN-based catalysts, a bimodal pore size distribution of 3.7 and 43.0 nm was observed. A marked decrease in pore volume was observed on Ni/MSN.

The summary data on surface areas and total pore volumes of all catalysts are listed in Table 1. In all cases, it can be seen that the surface area and total pore volume decreased considerably after the introduction of Ni, suggesting that a portion of the Ni particles were dispersed in the pores of the supports.

$^{27}$Al MAS NMR and $^{29}$Si MAS NMR offer a strong and effective tool for characterizing the structure of zeolite. In general, species with different structures or different chemical environments of the aluminum and silicon atoms will have different chemical shifts in their $^{27}$Al MAS NMR and $^{29}$Si MAS NMR spectra.[32] Fig. 3A and B show the $^{27}$Al MAS NMR and $^{29}$Si MAS NMR spectra of all catalysts, respectively. The $^{27}$Al MAS NMR was carried out to detect the presence of tetrahedral coordinated atoms (in the framework sites) and octahedral coordinated aluminum atoms (possibly as extra-framework aluminum, EFAL). As shown in Fig. 3A, three signals were observed for mZSM5: one signal at 61 ppm and two signals at around 0 ppm. A sharp resonance at 61 ppm corresponds to the tetrahedrally coordinated aluminum in the framework structure. This demonstrated that most of the aluminum atoms are incorporated into the zeolite framework. Additionally, two resonance signals were observed around 0 ppm, corresponding to the octahedral aluminum species in a highly symmetric environment and distorted octahedral aluminum species. For Ni/mZSM5, three signals were observed. A sharp signal at 59.5 ppm can be assigned to tetrahedral framework aluminum species. In addition, two octahedral aluminum species can be detected, both with an isotropic shift around 0 ppm, one type in a highly symmetric environment and one more distorted.[33] As compared with mZSM5, the intensity of the signal at around 0 ppm increased obviously may be due to the occurrence of dealumination during the calcination at 823 K, which then increased the extra-framework aluminum species.[34] On the other hand, only two signals were observed for HZSM5, at 56.5 and 0 ppm, which are attributed to tetrahedral and octahedral aluminum species, respectively. For Ni/HZSM5, two signals were observed at 55.6 and 0 ppm, corresponding to tetrahedral and octahedral aluminum species, respectively. For $Al_2O_3$-based catalysts (γ-$Al_2O_3$ and Ni/γ-$Al_2O_3$), two signals centered at 71.5 and 11 ppm were observed and can be assigned to tetrahedrally coordinated Al and octahedrally coordinated Al, respectively.[35] In Fig. 3B, only a dominant signal was observed at −106 ppm, which is assigned to the crystallographically equivalent site of $(\equiv SiO)_4Si$ for both mZSM5 and Ni/mZSM5.[32] No significance difference was observed upon the introduction of Ni. For HZSM5, a dominant signal was observed at −104.4 ppm. Additionally, two shoulder peaks appeared at −98 and −93.5 ppm, indicating the formation of $(\equiv SiO)_3Si$ and $(\equiv SiO)_2Si$, respectively. For MSN and Ni/MSN, three signals at −102, −93.5, and −84.5 ppm were observed, which can be assigned to $(\equiv SiO)_4Si$, $(\equiv SiO)_3Si$, and $(\equiv SiO)_2Si$, respectively.[32]

Fig. 4 shows the SEM images of mZSM5 and Ni/mZSM5. As illustrated in the images, mZSM5 possessed a smooth surface with a typical coffin-type morphology. Similarly, Ni/mZSM5 also had a coffin-type morphology but the surface was covered with some Ni metal. Xin *et al.* observed that the parent ZSM-5 had a smooth surface with typical coffin shape and uniform crystallite size of 1.5–2.5 μm.[36] In addition, Zhou *et al.* reported the synthesis of mesoporous ZSM-5 zeolite crystals by conventional hydrothermal treatment under stirring. Without stirring, conventional MFI morphology was quite smooth and no mesopores or growth steps on crystal surfaces were observed.[37] On the contrary, rough and moustache-like surfaces were observed with stirring. The authors proposed that this mesoporous ZSM-5 crystal contains a microporous coffin-shaped core crystal wrapped by a mesoporous shell composed of uniformly aligned zeolite nanocrystals.

## Intrinsic basicity of the catalysts

Infrared spectroscopy with probe molecules is commonly used for surface acidity and basicity characterizations.[38] In the present work, pyrrole was used as a probe molecule for basicity

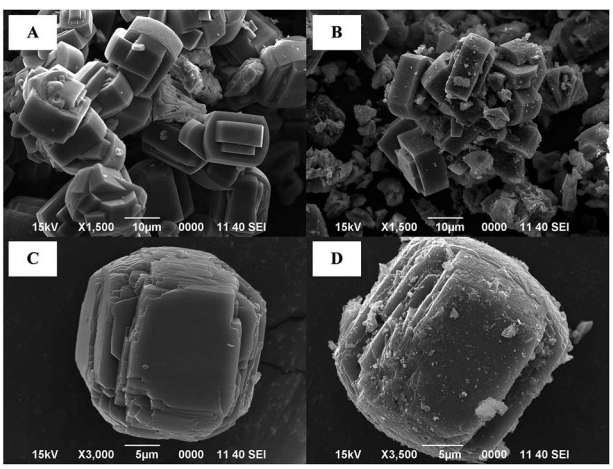


Fig. 4 SEM images of (A) mZSM5, (B) Ni/mZSM5, (C) closed up single particle of mZSM5, and (D) closed up single particle of Ni/mZSM5.

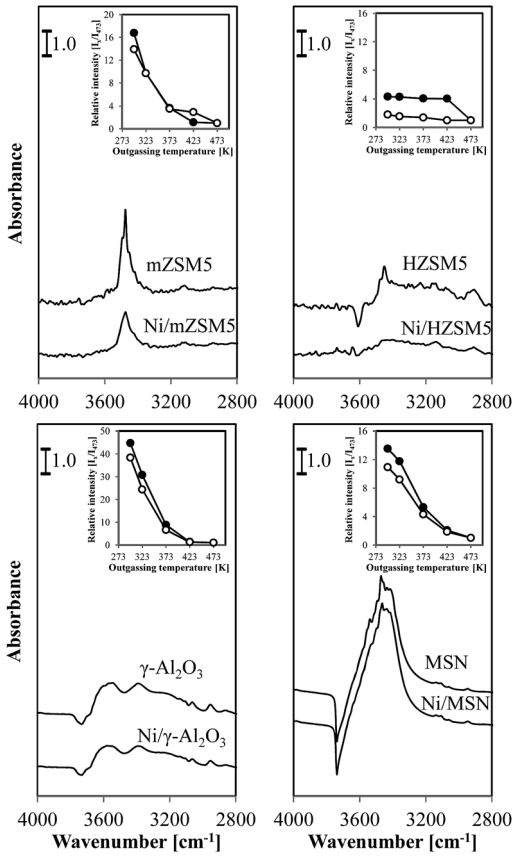


Fig. 5 FTIR spectra of pyrrole adsorbed on activated catalysts at room temperature, followed by heating in the vacuum at room temperature; the inset shows the relative intensity $I_x/I_{473}$, where $x$ = room temperature, 323 K, 373 K, 423 K, and 473 K. Basic sites (●) of mZSM5, HZSM5, $\gamma$-$Al_2O_3$, and MSN; basic sites (○) of Ni-promoted catalysts.

characterization. Fig. 5 shows the FTIR spectra of pyrrole adsorbed on activated catalysts in the N–H stretching region. For all catalysts, the main broad band situated in the region of 4000–2800 $cm^{-1}$ can be assigned to the N–H stretching vibrations of chemisorbed pyrrole ($C_4H_4NH$) interacting with the basic sites of framework oxygen atoms. The H-donor property of pyrrole allows the formation of $C_4H_4NH$–O bridges with basic oxygen. For zeolite-based catalysts, it also interacts *via* an aromatic system with the nonframework cations. Both interactions happen simultaneously and influence each other.[39] A sharp band at 3478 $cm^{-1}$ was observed for mZSM5, which is attributed to the perturbed N–H stretch of pyrrole molecules interacting with the surface of basic sites. Furthermore, the band at 3139 $cm^{-1}$ is attributed to the pyrrole in a liquid phase with medium strength, while the band at 2940 $cm^{-1}$ is assigned to a fundamental aliphatic $\nu$(CH) vibration.[40] An obvious reduction in the intensity of these peaks was observed for Ni/mZSM5. As a comparison with mZSM5-based catalysts, commercial HZSM5-based catalysts showed lower peak intensity, which indicates the lower basicity of the catalysts. In addition, $Al_2O_3$-based catalysts showed two bands at 3560 and 3380 $cm^{-1}$. The band at 3560 $cm^{-1}$ is attributed to surface hydroxyls interacting with the pyrrole ring, while the band appearing at 3380 $cm^{-1}$ is due to the N–H vibration of adsorbed species forming intermolecular bonds.[41] In the cases of MSN and Ni/MSN, the band at 3530 $cm^{-1}$ indicates the position of a pyrrole N–H band in the gas phase and the band at 3430 $cm^{-1}$ indicates the physisorbed pyrrole in a liquid-like state, where the N–H group interacts with the $\pi$-system of another pyrrole molecule.[42] The band at 3467 $cm^{-1}$ is attributed to the perturbed N–H stretch of pyrrole molecules interacting with the surface of basic sites.[22] The IR bands of adsorbed pyrrole on the Ni-promoted catalysts seem to be less intense than those of the corresponding supports. This suggests a decrease of the basicity as a result of the introduction of Ni. These results showed that Ni-promoted catalysts contained fewer available sites for the adsorption of pyrrole than the corresponding supports. This may be because the Ni metal sites block some of the pyrrole adsorption sites of the supports, leading to a decrease in CO adsorption on the catalysts.

## Catalytic performance

CO methanation was used to examine the catalytic activity of mZSM5, HZSM5, $\gamma$-$Al_2O_3$, MSN, and Ni-promoted catalysts in the temperature range of 423–673 K (Fig. 6A–C). For mZSM5, high methanation activity was only observed at high temperature (≥723 K), with a $CH_4$ yield of 42.9%.[21] The low methanation activity at <723 K for bare mZSM5 may be due to the absence of metal sites, which is crucial for the adsorption of CO and $H_2$ followed by spillover toward the support. However, without the support, Ni metal was also inactive in the CO methanation, which may be due to metal sintering. Li *et al.* reported that without $SiO_2$, sintering of Ni occurred, which led to low catalytic activity in $CO_2$ methanation.[43] Previously, we have reported the application of mZSM5 for both acid and base-catalyzed reactions, in which bare mZSM5-0.5D appeared to be the best catalyst for CO methanation. In this report, the presence of metal active sites such as Ni markedly enhanced the intrinsic properties of mZSM5 towards CO methanation. This indicated that metallic nickel is necessary for CO methanation over the studied system.

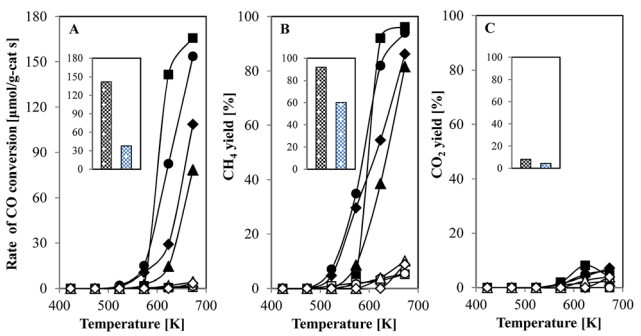


Fig. 6 (A) Rate of CO conversion, (B) yield of $CH_4$, and (C) yield of $CO_2$ as a function of the reaction temperature at GHSV = 13 500 ml $g^{-1}$ $h^{-1}$ and $H_2$/CO = 8/1. mZSM5 (□), Ni/mZSM5 (■), HZSM5 (◊), Ni/HZSM5 (♦), $\gamma$-$Al_2O_3$ (Δ), Ni/$\gamma$-$Al_2O_3$ (▲), MSN (○), and Ni/MSN (●). The inset shows catalytic performance of Ni/mZSM5 and Ni/ZSM5 at 623 K. Ni/mZSM5 (▩), and Ni/ZSM5 (▨).

Fig. 6A shows the rate of CO conversion for all catalysts as a function of the reaction temperatures. The activity of all Ni-promoted catalysts showed an obvious increase with increasing temperature. It is noteworthy that the catalytic performance of Ni/mZSM5 was superior compared to that of other Ni-promoted catalysts (Ni/MSN, Ni/HZSM5, and Ni/$\gamma$-$Al_2O_3$); it presents a significant catalytic activity (rate of CO conversion = 141.6 μmol CO g-cat$^{-1}$ s$^{-1}$) at 623 K. Additionally, Ni/mZSM5 exhibited the highest yield of $CH_4$ of 92.0% at 623 K, which increased notably to 96.1% at 673 K, as demonstrated in Fig. 6B. Meanwhile, Ni/MSN only gave 82.4 μmol CO g-cat$^{-1}$ s$^{-1}$ and 82% $CH_4$ yield, Ni/HZSM5 gave 29.0 μmol CO g-cat$^{-1}$ s$^{-1}$ and 54.5% $CH_4$ yield, and Ni/$\gamma$-$Al_2O_3$ gave 14.5 μmol CO g-cat$^{-1}$ s$^{-1}$ and 38.6% $CH_4$ yield at 623 K. Besides, Ni-promoted ZSM5 (Ni/ZSM5) gave 37.5 μmol CO g-cat$^{-1}$ s$^{-1}$ and 60.3% $CH_4$ yield (inset figure in Fig. 6). As shown in Fig. 6C, only a small amount of $CO_2$ (<10%) was produced for all catalysts under the reaction temperatures studied. These results showed that the existence of Ni metal sites inhibited the water–gas shift reaction of CO to $CO_2$ and favored the methanation reaction. The presence of low $CO_2$ yield for all Ni-promoted catalysts corroborates this suggestion.

It is noteworthy that our results are up to par with previous reported literature reviews (Table 2). Derekaya and Yasar reported CO methanation over NaY–zeolite in which Ni/$ZrO_2$/NaY appeared to be the most active catalyst with 100% conversion at 548 K.[44] In addition, Ding *et al.* reported the high activity of Ni/$Al_2O_3$–$CeO_2$ with 91.6% CO conversion, 92% $CH_4$ selectivity, and 84% $CH_4$ yield at 623 K.[45] Moreover, Variava *et al.* studied carbon-nanotube supported catalysts for $CH_4$ production.[46] Based on their results, 13 wt% Ni/MWNT achieved the highest activity with ~95% CO conversion, ~85% $CH_4$ selectivity, and ~81% $CH_4$ yield at 623 K. Shinde *et al.* reported the implementation of 23 wt% Ni/$TiO_2$ for $CH_4$ production.[47] They studied the sonication and conventional impregnation methods, and the former showed higher activity for $CH_4$ formation, with ~99% CO conversion, 88% $CH_4$ selectivity, and 87% $CH_4$ yield at 593 K.

Recently, we reported a study of mesoporous ZSM5 having both intrinsic acidic and basic sites for cracking and methanation and we concluded that the co-existence of micro–mesoporosity with the presence of inter- and intra-particle pores and dual intrinsic acidic–basic sites is vital for acid-catalyzed and base-catalyzed reactions. In the present work, we focus on base-catalyzed CO methanation reaction for methane production. Fig. 7 shows the relationship of the basic sites with the catalytic activity at 623 K. Conversion of carbon monoxide to methane is essentially catalyzed by the support over the basic sites and therefore the presence of these basic sites is a key point in CO methanation to produce methane. With bare support, the presence of basic sites did not show any significance effect on the catalytic performance (rate of CO conversion and yield of $CH_4$ and $CO_2$). However, the catalytic activity is enhanced in the presence of Ni metal active sites and thus a synergistic effect of Ni metal active sites and mZSM5 support could be claimed to occur. Results from pyrrole adsorbed FTIR (Fig. 5) showed that the concentration of basic sites in Ni/mZSM5 is higher than in Ni/HZSM5 and Ni/$\gamma$-$Al_2O_3$ catalysts but lower than in Ni/MSN. Notably, an optimum amount of basic sites is needed to obtain a high yield of methane. These results are in accordance with other studies reported in the literature.[31,48,49]

## Mechanistic investigation of CO methanation

The nature of the active sites and reaction mechanisms for CO methanation has been a longstanding topic in heterogeneous catalysis. There is a lot of controversy regarding these issues. Two possible mechanisms for CO methanation have been

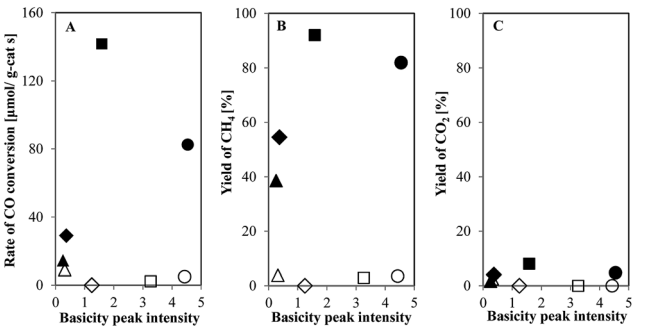


Fig. 7 Relationship of basicity–catalytic activity at 623 K (A–C). mZSM5 (□), Ni/mZSM5 (■), HZSM5 (◊), Ni/HZSM5 (♦), $\gamma$-$Al_2O_3$ (Δ), Ni/$\gamma$-$Al_2O_3$ (▲), MSN (○), and Ni/MSN (●). Empty symbol in (A) is multiple 5 times the original value.

Table 2 Comparison study of Ni-promoted catalysts

| | Catalytic performance [%] | | | Reaction conditions | | |
|---|---|---|---|---|---|---|
| Catalyst | CO conversion | $CH_4$ selectivity | $CH_4$ yield | Temperature [K] | Pressure [MPa] | Reference |
| Ni/mZSM5 | 100 | 92 | 92 | 623 | 0.1 | This study |
| Ni/HZSM5 | 59 | 93 | 54 | 623 | 0.1 | This study |
| Ni/$\gamma$-$Al_2O_3$ | 40 | 96 | 39 | 623 | 0.1 | This study |
| Ni/MSN | 87 | 95 | 82 | 623 | 0.1 | This study |
| Ni/$ZrO_2$/NaY | 100 | — | — | 548 | — | 44 |
| Ni/$Al_2O_3$–$CeO_2$ | 91.6 | 92 | 84 | 623 | 0.1 | 45 |
| Ni/MWNT | ~95 | ~85 | ~81 | 623 | 0.1 | 46 |
| Ni/$TiO_2$ | ~99 | 88 | 87 | 613 | 0.1 | 47 |

proposed, that is, a direct CO dissociation mechanism and a hydrogen-assisted CO dissociation mechanism.[50]

The FTIR adsorption spectra of CO + $H_2$ adsorption on mZSM5 and Ni/mZSM5, the interaction of $H_2$ with pre-adsorbed CO, and the interaction of CO with pre-adsorbed $H_2$ on Ni/mZSM5 are presented in Fig. 8. The blank reaction (without catalyst) of CO + $H_2$ showed no significant peak, which showed that adsorbed species is needed for the methanation reaction. Furthermore, the adsorption of CO + $H_2$ on Ni showed no IR adsorption peak as the experiment could not proceed because the Ni pellet became black after being reduced by the hydrogen flow. As mentioned earlier, CO methanation on Ni was negligible, indicating that a methanation reaction was probably not taking place on the Ni surface. For *in situ* FTIR spectroscopy of CO + $H_2$ (Fig. 8A and B), the adsorption bands at 2170 and 2110 $cm^{-1}$ were observed for both mZSM5 and Ni/mZSM5 catalysts, which can be assigned to the gaseous CO. A band at 1625 $cm^{-1}$ was observed on mZSM5, which was assigned to atomic hydrogen. It can be suggested that bare mZSM5 has a low ability to adsorb and dissociate molecular hydrogen to atomic hydrogen. From our previous results, it is known that high methanation activity over mZSM5 only happens at high temperature (at 723 K). Therefore, in the present study, Ni metal was introduced to mZSM5 support to convert gaseous CO and $H_2$ to adsorbed species on mZSM5 support, which allowed high interaction between the two reactants and lowered the reaction temperature. A band was observed at 1850 $cm^{-1}$ and shifted to 1810 $cm^{-1}$ at higher temperature, indicating the presence of adsorbed carbonyls on $Ni^0$ sites ($Ni^0$–CO) on the Ni/mZSM5.[51,52] The band at 1850 $cm^{-1}$ shifted to 1810 $cm^{-1}$ upon temperature increase, which is likely caused by the destabilization of $Ni^0$–CO species. This may also be due to the CO desorption from more labile adsorption on Ni sites. Moreover, the evolution of the adsorption band at 1625 $cm^{-1}$ is attributed to the presence of atomic hydrogen. Furthermore, the formation of adsorbed carbonate species was only observed on Ni/mZSM5, as evidenced by the adsorption bands at 1510 and 1360 $cm^{-1}$.[53] At 623 K, Ni/mZSM5 showed a fully diminished in gaseous CO bands, a notable depletion in $Ni^0$–CO bands, and progressive formation of carbonate species. At this temperature, the system's energy starts to be high enough for it to dissociate and then hydrogenate or to hydrogenate CO directly until methane formation.

In order to clarify the predominant reaction pathway for CO methanation over Ni/mZSM5, the interaction of $H_2$ with pre-adsorbed CO and interaction of CO with pre-adsorbed $H_2$ was examined by *in situ* FTIR (Fig. 8C and D). In the study of the interaction of $H_2$ with pre-adsorbed CO, four adsorption bands were observed at 1780, 1625, 1510 and 1360 $cm^{-1}$. The band at 1780 $cm^{-1}$, which was assigned to $Ni^0$–CO species, was significantly decreased at 623 K. No obvious changes of the other three adsorption bands were observed. On the other hand, in the study of the interaction of CO with pre-adsorbed $H_2$, the results showed one additional adsorption band at 2340 $cm^{-1}$, which was assigned to gaseous $CO_2$. $CO_2$ species may result from the interaction of the adsorbed CO with the oxide surface of mZSM5 or as a consequence of the water–gas shift reaction and accumulation on the support. With increasing temperature,

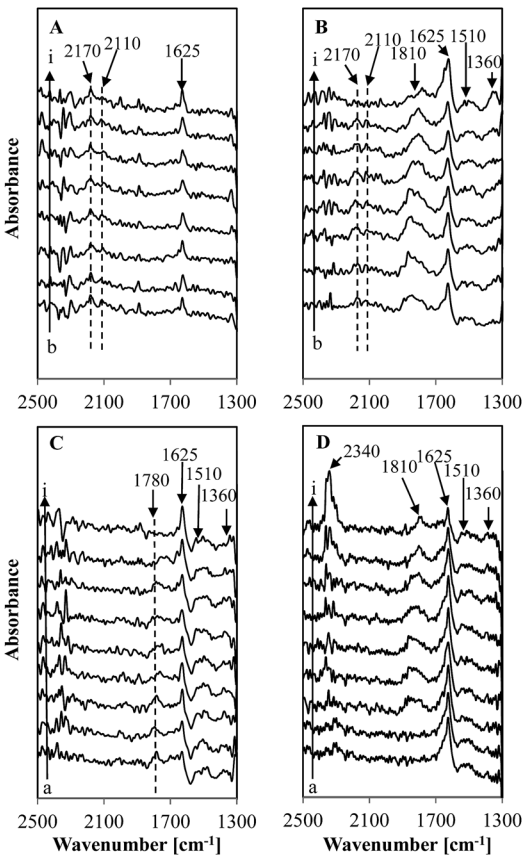


Fig. 8 Evaluation of the FTIR spectra of adsorbed gases (CO + $H_2$) on (A) mZSM5, (B) Ni/mZSM5, (C) interaction of $H_2$ with pre-adsorbed CO Ni/mZSM5, and (D) interaction of CO with pre-adsorbed $H_2$ Ni/mZSM5. The samples were heating up to (b) room temperature, (c) 323 K, (d) 373 K, (e) 423 K, (f) 473 K, (g) 523 K, (h) 573 K, and (i) 623 K. (a) pre-adsorbed CO (for C) or pre-adsorbed $H_2$ (for D) on Ni/mZSM5 at room temperature.

reduction of the adsorption bands of $Ni^0$–CO and atomic hydrogen at 1810 and 1625 $cm^{-1}$, respectively, were observed. Moreover, a methanation reaction can occur on the $Ni^0$ sites as well as on the mZSM5 support. However, in this case, the methanation sites on the mZSM5 support are more active as compared to the ones on the $Ni^0$ sites. From these results, we can propose two possible mechanisms for CO methanation. In the first mechanism, the adsorbed CO species may be reacted with $H_2$ to form $CH_4$ and $H_2O$. In the second mechanism, the adsorbed H may be reacted with CO to form $CH_4$ and $CO_2$. However, in this case, the former is the predominant pathway as the methanation reaction is favored by inhibition of the water–gas shift reaction. Therefore, a plausible reaction mechanism of CO methanation over Ni/mZSM5 is shown in Scheme 1.

Under the experimental conditions used in the present work, the presence of metal carbonyl ($Ni^0$–CO) was observed. This may suggest that the route to methane formation was formed *via* metal carbonyl. Unfortunately, in this experiment, the $CH_x$ vibration bands in the 2800–3000 $cm^{-1}$ region were not detected for these catalysts. Chen *et al.* studied the reaction mechanism of Si–Ni/$SiO_2$ catalyst by temperature-programmed

 

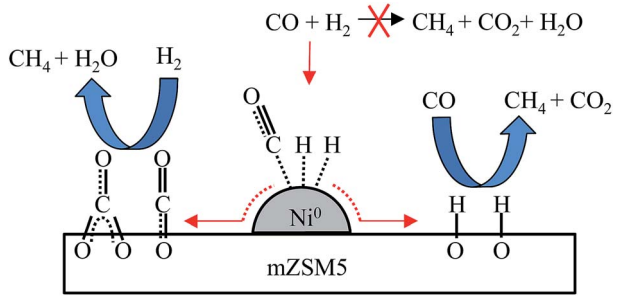


Scheme 1 Plausible reaction mechanism of CO methanation over Ni/mZSM5.

reaction FTIR (TPR-FTIR) and temperature-programmed desorption FTIR (TPD-FTIR).[51] From their results, three possible mechanisms emerged: (1) the gas phase CO was initially absorbed on the surface of nickel silicide as a linear- and bridge-type species; (2) the bridge-type CO was easily dissociated to $C_s$ (adsorbed carbon) and $CO_2$ on the surface of nickel silicide; and (3) the linearly adsorbed CO and the $C_s$ were then quickly reacted with dissociated hydrogen ($H_s$) to form the $CH_4$. Zarfl *et al.* reported on the DRIFTS study of commercial Ni/$\gamma$-$Al_2O_3$ for CO methanation.[54] They suggested that atomic C and H produced by CO and $H_2$ dissociation on Ni during methanation and C–H species may recombine to form methane product. However, these experimental results cannot confirm the role of hydrogenation of adsorbed CO species. Zhang *et al.* proposed a mechanism of carbon monoxide methanation on a Ru(0001) surface based on a density functional theory (DFT) study.[2] Their result showed that the reaction pathway for CO methanation proceeds *via* either a COH or a CHO intermediate from CO dissociation, resulting in active C and CH species, respectively. The active C and CH species subsequently undergo stepwise hydrogenation to $CH_4$. Zhen *et al.* studied $CO_2$ methanation on Ni–Ru/$\gamma$-$Al_2O_3$ and proposed that $CO_2$ was dissociated on Ru species surfaces to form carbon species ($CO_{ads}$) and oxygen species ($O_{ads}$) and then reacted with activated H on Ni centers to form methane and water.[55] However, the role of Ni and Ru species was not discussed in detail. Besides, the methanation reaction can also proceed through a hydrogen-assisted CO dissociation mechanism (formate route), which has been proposed in the literature.[56,57] However, in the present work, the absence of formate species suggested that it is not a possible route for CO methanation over mZSM5-based catalyst.

## Conclusions

A structurally stable nickel-promoted mesoporous ZSM5 (Ni/mZSM5) was prepared for CO methanation. Ni/mZSM5 was found to be highly active for CO methanation, with a high rate of CO conversion (141.6 μmol CO g-cat$^{-1}$ s$^{-1}$) and 92% $CH_4$ yield at a relatively low temperature of 623 K. Ni/mZSM5 showed superior catalytic performance compared to Ni/MSN, Ni/HZSM5, and Ni/$\gamma$-$Al_2O_3$. In this case, the presence of Ni, micro-mesoporosity, and basicity is of crucial significance. Additionally, the introduction of Ni provokes a synergistic effect between the metal active sites and the mZSM5 support. Based on *in situ* FTIR studies, CO and $H_2$ may be adsorbed on Ni metal followed by migration onto the mZSM5 surface to form adsorbed CO and adsorbed H. Then, two possible mechanisms for CO methanation were proposed. In the first mechanism, the adsorbed CO may be reacted with $H_2$ to form $CH_4$ and $H_2O$. In the second mechanism, the adsorbed H may be reacted with CO to form $CH_4$ and $CO_2$. However, in this case, the former is the predominant pathway as the methanation reaction is favored by the inhibition of the water–gas shift reaction.

## Acknowledgements

This work was supported by the Universiti Teknologi Malaysia through Research University Grant No. 06H17 and MyPhd Scholarship (Teh Lee Peng) from the Ministry of Higher Education, Malaysia.

## References

1 P. Sabatier and J. B. Senderens, *Compt. Rend. Acad. Sci.*, 1902, **134**, 514.
2 S.-T. Zhang, H. Yan, M. Wei, D. G. Evans and X. Duan, *RSC Adv.*, 2014, **4**, 30241.
3 H. Yoshida, K. Watanabe, N. Iwasa, S.-I. Fujita and M. Arai, *Appl. Catal., B*, 2015, **162**, 93.
4 J. Gao, Q. Liu, F. Gu, B. Liu, Z. Zhong and F. Su, *RSC Adv.*, 2015, **5**, 22759.
5 X. Yan, Y. Liu, B. Zhao, Z. Wang, Y. Wang and C.-J. Liu, *Int. J. Hydrogen Energy*, 2013, **38**, 2283.
6 C. Guo, Y. Wu, H. Qin and J. Zhang, *Fuel Process. Technol.*, 2014, **124**, 61.
7 Q. Liu, F. Gua, X. Lu, Y. Liu, H. Li, Z. Zhong, G. Xua and F. Su, *Appl. Catal., A*, 2014, **488**, 37.
8 J. Zhang, Z. Xin, X. Meng and M. Tao, *Fuel*, 2013, **109**, 693.
9 J. Gao, C. Jia, M. Zhang, F. Gu, G. Xu, Z. Zhong and F. Su, *RSC Adv.*, 2013, **3**, 18156.
10 C. Jia, J. Gao, J. Li, F. Gu, G. Xu, Z. Zhong and F. Su, *Catal. Sci. Technol.*, 2013, **3**, 490.
11 P. Panagiotopoulou and D. I. Kondarides, *Catal. Today*, 2006, **112**, 49.
12 J. Wang, P. A. Chernavskii, Y. Wang and A. Y. Khodakov, *Fuel*, 2013, **103**, 1111.
13 J. Kugai, T. Moriya, S. Seino, T. Nakagawa, Y. Ohkubo, H. Nitani, K. Ueno and T. A. Yamamoto, *J. Phys. Chem. C*, 2013, **117**, 5742.
14 R. Liu, Y. Zhu, Z. Sui, H. Wang, P. Li and X. Zhou, *Fuel Process. Technol.*, 2013, **108**, 82.
15 A. Primo and H. Garcia, *Chem. Soc. Rev.*, 2014, **43**, 7548.
16 M. Sánchez-Sánchez and T. Blasco, *Catal. Today*, 2009, **143**, 293.
17 Z. Wang, P. Dornath, C.-C. Chang, H. Chen and W. Fan, *Microporous Mesoporous Mater.*, 2013, **181**, 8.
18 B. Liu, L. Zheng, Z. Zhu, C. Li, H. Xi and Y. Qian, *Appl. Catal., A*, 2014, **470**, 412.

19 P. Panagiotopoulou, D. I. Kondarides and X. E. Verykios, *Appl. Catal., A*, 2008, **344**, 45.
20 S. Tada, R. Kikuchi, A. Takagaki, T. Sugawara, S. T. Oyawa and S. Satokawa, *Catal. Today*, 2014, **232**, 16.
21 L. P. Teh, S. Triwahyono, A. A. Jalil, R. R. Mukti, M. A. A. Aziz and T. Shishido, *Chem. Eng. J.*, 2015, **270**, 196.
22 M. A. A. Aziz, A. A. Jalil, S. Triwahyono, R. R. Mukti, Y. H. Taufiq-Yap and M. R. Sazegar, *Appl. Catal., B*, 2014, **147**, 359.
23 M. M. J. Treacy and J. B. Higgins, *Collection of Simulated XRD Powder Patterns for Zeolites*, Elsevier, New York, 4th edn, 2001.
24 X. Chen, Y. Cheng, C. Yup Seo, J. W. Schwank and R. W. McCabe, *Appl. Catal., B*, 2015, **163**, 499.
25 T. K. Phung, A. Lagazzo, M. A. R. Crespo, V. S. Escribano and G. Busca, *J. Catal.*, 2014, **311**, 102.
26 J. Zhang, Z. Xin, X. Meng, Y. Lv and M. Tao, *Fuel*, 2014, **116**, 25.
27 M. Guo and G. Lu, *RSC Adv.*, 2014, **4**, 58171.
28 A. H. Karim, A. A. Jalil, S. Triwahyono, N. H. N. Kamarudin and A. Ripin, *J. Colloid Interface Sci.*, 2014, **421**, 93.
29 H. P. Decolatti, B. O. D. Costa and C. A. Querini, *Microporous Mesoporous Mater.*, 2015, **204**, 180.
30 S. S. Akarmazyan, P. Panagiotopoulou, A. Kambolis, C. Papadopoulou and D. I. Kondarides, *Appl. Catal., B*, 2014, **145**, 136.
31 X. Dai, J. Liang, D. Ma, X. Zhang, H. Zhao, B. Zhao, Z. Guo, F. Kleitz and S. Qiao, *Appl. Catal., B*, 2015, **165**, 752.
32 J. Klinowski, *Colloids Surf.*, 1989, **36**, 133.
33 W. Luo, U. Deka, A. M. Beale, E. R. H. van Eck, P. C. A. Bruijnincx and B. M. Weckhuysen, *J. Catal.*, 2013, **301**, 175.
34 P. Wu, T. Komatsu and T. Yashima, *J. Phys. Chem.*, 1995, **99**, 10923.
35 H. Li, M. Li and H. Nie, *Microporous Mesoporous Mater.*, 2014, **188**, 30.
36 H. Xin, X. Li, Y. Fang, X. Yi, W. Hu, Y. Chu, F. Zhang, A. Zheng, H. Zhang and X. Li, *J. Catal.*, 2014, **312**, 204.
37 M. Zhou, A. A. Rownaghi and J. Hedlund, *RSC Adv.*, 2013, **3**, 15596.
38 G. Busca, *Heterogeneous Catalytic Materials: Solid State Chemistry, Surface Chemistry and Catalytic Behaviour*, Elsevier, Amsterdam, 2014.
39 H. Förster, H. Fuess, E. Geidel, B. Hunger, H. Jobic, C. Kirschhock, O. Klepel and K. Krause, *Phys. Chem. Chem. Phys.*, 1999, **1**, 593.
40 J. C. Lavalley, *Catal. Today*, 1996, **27**, 377.
41 P. Berteau, S. Ceckiewicz and B. Delmon, *Appl. Catal.*, 1987, **31**, 361.
42 B. Camarota, Y. Goto, S. Inagaki and B. Onida, *Langmuir*, 2011, **27**(3), 1181.
43 Y. Li, G. Lu and J. Ma, *RSC Adv.*, 2014, **4**, 17420.
44 F. B. Derekaya and G. Yaşar, *Catal. Commun.*, 2011, **13**, 73.
45 M.-Y. Ding, J.-Y. Tu, T.-J. Wang, L.-L. Ma, C.-G. Wang and L.-G. Chen, *Fuel Process. Technol.*, 2015, **134**, 480.
46 M. F. Variava, T. L. Church, N. Noorbehesht, A. T. Harris and A. I. Minett, *Catal. Sci. Technol.*, 2015, **5**, 515.
47 V. M. Shinde and G. Madras, *AIChE J.*, 2014, **60**, 1027.
48 Y. Wei, J. Liu, Z. Zhao, C. Xu, A. Duan and G. Jiang, *Appl. Catal., A*, 2013, **453**, 250.
49 H. Zhang, H. Qiao, H. Wang, N. Zhou, J. Chen, Y. Tang, J. Li and C. Huang, *Nanoscale*, 2014, **6**, 10235.
50 J.-X. Liu, H.-Y. Su and W.-X. Li, *Catal. Today*, 2013, **215**, 36.
51 X. Chen, J. Jin, G. Sha, C. Li, B. Zhang, D. Su, C. T. Williams and C. Liang, *Catal. Sci. Technol.*, 2014, **4**, 53.
52 A. Westermann, B. Azambre, M. C. Bacariza, I. Graça, M. F. Ribeiro, J. M. Lopes and C. Henriques, *Appl. Catal., B*, 2015, **174**, 120.
53 S. C. Shen, X. Chen and S. Kawi, *Langmuir*, 2004, **20**, 9130.
54 J. Zarfl, D. Ferri, T. J. Schildhauer, J. Wambach and A. Wokaun, *Appl. Catal., A*, 2015, **495**, 104.
55 W. Zhen, B. Li, G. Lu and J. Ma, *RSC Adv.*, 2014, **4**, 16472.
56 Q. Pan, J. Peng, S. Wang and S. Wang, *Catal. Sci. Technol.*, 2014, **4**, 502.
57 M. A. A. Aziz, A. A. Jalil, S. Triwahyono and S. M. Sidik, *Appl. Catal., A*, 2014, **486**, 115.